Mon. Not. R. Astron. Soc. **348,** 1065–1077 (2004) doi:10.1111/j.1365-2966.2004.07430.x

The infrared continuum of active galactic nuclei

M. Contini,[1]★ S. M. Viegas[2] and M. A. Prieto[3]

[1]*School of Physics and Astronomy, Tel Aviv University, Tel Aviv 69978, Israel*
[2]*Instituto de Astronomia, Geofísica e Ciências Atmosféricas – USP, Brazil*
[3]*Max-Planck-Institut für Astronomie, Königstuhl 17, D-69117, Heidelberg, Germany*

Accepted 2003 November 16. Received 2003 November 7; in original form 2003 September 12

ABSTRACT

We discuss the different physical processes contributing to the infrared continuum of active galactic nuclei (AGNs), assuming that both photoionization from the active centre and shocks ionize and heat the gas and dust contained in an ensemble of clouds surrounding the nucleus. In our model, radiation transfer of primary and secondary radiation throughout a cloud is calculated consistently with collisional processes due to the shock. We consider that the observed continuum corresponds to reprocessed radiation from both dust and gas in the clouds. Collisional processes are important in the presence of shocks. The grains are sputtered crossing the shock front. The models are constrained by sputtering as well as by the far-infrared data. The model is applied to the continuum of Seyfert galaxies from which the best estimate of the nuclear, stellar subtracted, emission is available. The results show that radiation-dominated high-velocity clouds are more numerous in Seyfert 1–1.5 whereas shock-dominated low-velocity clouds are dominant in Seyfert type 2. This result is in full agreement with the unified model for AGNs, by which high-velocity clouds, placed deeper into the central region and therefore reached by a more intense radiation, should play a more significant role in the spectra of broad-line objects. We could therefore conclude that in type 2 objects, radiation is partly suppressed by a central dusty medium with a high dust-to-gas ratio. Once the model approach is tested, a grid of models is used to provide a phenomenological analysis of the observed infrared spectral energy distribution. This empirical method is a useful tool to rapidly access the physical conditions of the AGN emitting clouds. For this, analytical forms are derived for the two processes contributing to the infrared emission: dust emission and thermal bremsstrahlung produced by the narrow-line region clouds. Their relative contribution provides a measurement of the dust-to-gas ratio.

Key words: galaxies: active – galaxies: nuclei – galaxies: Seyfert – infrared: galaxies.

1 INTRODUCTION

The presence of a dusty torus around the central engine was proposed by Antonucci & Miller (1985) to explain the broad emission lines observed in the polarized light of Seyfert 2 galaxies. The torus absorbs a large fraction of the nuclear emission and reradiates it in the infrared (IR). This is the basis of the so-called active galactic nucleus (AGN) unification scheme, largely analysed in the literature, which provides a geometrical explanation for the observed differences between broad-line and narrow-line objects.

After the pioneering work by Edelson & Malkan (1986), the characteristics of the continuum due to dust heated by the optical–ultraviolet (UV) nuclear radiation have been analysed by several authors (Barvainis 1992; Pier & Krolik 1992; Laor & Draine 1993; Granato & Danese 1994; Granato, Danese & Franceschini 1997; Nenkova, Ivezić & Elitzur 2002).

The IR emission is generally associated with a dusty torus surrounding the central source of the AGN. Although proposed by Pier & Krolik (1992, 1993), the calculation of the radiative transfer radiation throughout a clumpy torus has only recently been performed by Nenkova et al. (2002). The AGN obscuring region is modelled as a toroidal distribution of dusty clouds placed at different radii from the centre, each with the same optical depth. The optically thick clumps are heated by the nuclear radiation as well as by the radiation originated in other clumps. The dust temperature is much higher in their illuminated side. The authors claim that heating by diffuse radiation is highly inefficient and can be neglected. Following their results, a clumpy torus accounts for both the often observed broad IR bump extending up to 100 μm and the absence of the 10-μm silicate feature in type 1 – on-axis view – objects.

In general, two types of model are used in the literature: a compact torus (radial dimension smaller than a few pc) with a large optical

★E-mail: contini@post.tau.ac.il

depth, and a more extended (up to hundreds of pc) moderately thick disc. A common characteristic to all is that dust survival in the vicinity of the AGN is set by its evaporation limit. Therefore, dust can reach temperatures up to 1000–1500 K. Overall, these models provide a reasonable fit to the observed spectral energy distribution (SED). The torus models usually assume a high equatorial opacity leading to flat spectra for type 1 galaxies and steep spectra for type 2 galaxies. However, as pointed out by Alonso-Herrero et al. (2003), the large number of spectral indices observed in both types of galaxies, as well as the large number of intermediate and type 1 objects with steep SEDs, cannot be explained by the torus model.

Other simpler descriptions of the IR SED include, for example, that by Blain, Barnard & Chapman (2003) who describe the far-infrared (FIR) to submillimetre SED of dusty galaxies with different forms of modified blackbody models.

Although most available models provide, in one way or another, a fair representation of the IR SED, we believe that a more sound physical approach is needed. An important problem affecting all these models, those mentioned above, as well as in the approach of Blain et al. (2003), is that the results are independent of the dust-to gas ratio.

For several years, we have been pursuing the development of self-consistent models aimed at explaining both the emission-line and SED of AGNs. These models have proved to be successful in a number of representative Seyfert galaxies (Contini, Prieto & Viegas 1998a,b; Contini, Viegas & Prieto 2002). In our modelling approach, the IR–optical continuum is due to dust emission and free–free emission from the clouds powered by the nuclear radiation, diffuse radiation and by shocks. Shocks are due to the cloud motion through a dilute gas (Contini & Viegas-Aldrovandi 1990; Viegas & Contini 1994; Contini & Viegas 2000). An important aspect considered in that approach is the conditions of dust survival when effects such as sputtering and grain–gas collisions are taken on board. Thus, these models offer an alternative to the torus model, particularly for objects showing IR emission as extended as the narrow-line region (NLR).

Overall, we consider a model to be well constrained when both the complete SED and the emission-line spectrum are simultaneously modelled. When possible, this has been our approach, for example, in the references quoted above. However, in this paper, we focus on the optical–IR continuum only, because in this wavelength range the best estimate of the nuclear flux emission, and of shock velocities for a reasonable number of Seyfert galaxies of different types (the sample by Alonso-Herrero et al. 2003), is available.

The paper is structured as follows. A short review of the processes involving dust is given in Section 2. In Section 3, numerical simulations accounting for the presence of both shocks and photoionization in the NLR are presented and applied to the SEDs of Seyfert galaxies, described in Alonso-Herrero et al. (2003). Concluding remarks appear in Section 4. In the Appendix, we present an empirical method derived from the models, aimed at providing a first assessment of the nature of the observed IR continuum.

2 DUST AND GAS EMISSION

When the physical conditions of a dust cloud are due to a combination of photoionization and shock, the dust heating and temperature will depend on the UV radiations as well as on the post-shock temperature.

The maximum grain temperature, which would account for the near-IR emission, is limited by sublimation. An estimate for some Seyfert 2 galaxies shows that the critical distance for grain survival, i.e. the distance where the grain temperature is equal to the evaporation temperature, for both graphite and silicate, is in the range 0.25–50 pc, depending on the luminosity of the central source (Vaceli et al. 1993). In addition, the value of the temperature reached by the grains depends on the presence of small grains and on a strong UV radiation from the central source.

Several lines of evidence point towards the destruction of very small grains in regions of high UV radiation intensity (Rowan-Robinson 1992). The destruction of dust by these effects is relevant when gas velocities about or larger than 300 km s^{-1} are present; still, velocities of $\geqslant$100 km s^{-1} can have an effect on dust destruction as we shall see below.

In the following, we review the effect of photoionization and shocks on the temperature and survival of dust grains in an emitting cloud of the NLR.

2.1 Description of our models: the code SUMA

Our models result from numerical simulations with the code SUMA (Viegas & Contini 1994, 1997, and references therein) which requires the following input parameters: the shock velocity, V_s, the pre-shock density, n_0, the pre-shock magnetic field, B_0, an ionizing radiation spectrum, the chemical composition of the gas and a dust-to-gas ratio d/g. As ionizing continuum, we consider a power law characterized by the ionizing flux at the Lyman limit F_h (in photons cm^{-2} s^{-1} eV^{-1}) and a spectral index, or a combination of spectral indices in different wavelength ranges. A plan-parallel symmetry is adopted with the calculations starting at the shocked edge and the cloud divided in slabs. The number of slabs is chosen according to the precision required by the calculation of the physical conditions. The geometrical thickness of the cloud, D, is also an input parameter in the case where shock and photoionization act on the opposite edges of the cloud. This is the common case for clouds flowing outward from the nucleus.

The models discussed here have been obtained assuming a spectral index of 1.5, cosmic chemical abundances for He, C, N, O, Ne, Mg, Si, S, Ar and Fe (Allen 1973), and $B_0 = 10^{-4}$ G. The other input parameters are variable in ranges established by the observations as well as by previous modelling of the NLR.

As the calculations account for the sputtering in the different zone downstream of the shock front (Viegas & Contini 1994), the distribution of the grain sizes along the cloud is automatically derived by SUMA starting from an initial size. In AGNs, carbon and polycyclic aromatic hydrocarbon (PAH) grain features are relatively less prominent than, for example, in starburst galaxies; therefore, only silicate grains are considered (Siebenmorgen, Kruegel & Spoon 2003).

Self-consistent calculations lead to the continuum and emission-line spectra which are compared with the data.

2.2 Description of our models: the IR emission

Like Nenkova et al. (2002), we also consider an ensemble of dusty clouds placed at different distances from the active centre. In our model, radiation transfer of primary and secondary radiation throughout a cloud is calculated consistently with collisional processes due to the shock. Moreover, we consider that the observed continuum corresponds to reprocessed radiation from both dust and gas in the clouds. For NLR clouds moving outwards, in the edge of the cloud facing the photoionizing source, dust and gas are mainly heated by the primary radiation, although the effect of the diffuse radiation from the ionized gas cannot be neglected. Collision effects are less important because they increase with temperature, which is

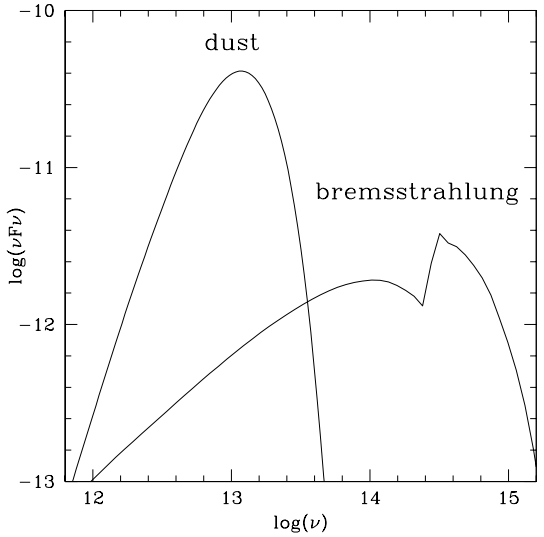

Figure 1. The dust re-emission peak relative to bremsstrahlung emission for a prototype model M3 (Table 1).

usually smaller in the photoionized region. The temperature of the gas, in fact, does not exceed 2–3 $\times$ 10^4 K in this region.

On the other hand, at the opposite edge, the gas is collisionally heated to relatively high temperatures by the shock. The post-shock temperatures depend on the shock velocity ($\propto V_s^2$). In these models, dust and gas are coupled throughout the shock front. Collision phenomena dominate at high temperature leading to relatively high temperatures of gas and grains. Diffuse radiation from the hot gas bridges between the shock-dominated and the radiation-dominated sides of the cloud.

The structure of the gas downstream is determined by the shock. In fact, the density distribution results from compression and the temperature distribution is strongly affected by the cooling rate. Due to gas and dust mutually heating and cooling, the maximum temperature of dust depends on the shock velocity, which therefore determines the frequency of the reradiation peak in the IR. An analytical relation between the wavelength of the maximum intensity of dust reradiation in the IR spectrum and shock velocity is given by Draine (1981).

The hot NLR clouds produce bremsstrahlung. Depending on the temperature distribution in the cloud, this mechanism may contribute to the IR continuum (see, for instance, Contini & Viegas-Aldrovandi 1990, fig. 2c). The intensity of dust IR emission relative to bremsstrahlung depends on the dust-to-gas ratio d/g. Usually the dust contribution dominates in the FIR range but in the near-IR, both processes may contribute to the continuum as shown in Fig. 1, where the single-cloud continuum of model M3 (Table 1) is plotted.

Table 1. The input parameters of single-cloud models.

Model	M1	M2	M3	M4	M5	M6	M7
V_s (km s^{-1})	100	500	500	500	500	700	1000
n_0 (cm^{-3})	1000	300	300	300	300	300	1000
log(F_h)	–	11	11	11	–	–	11
D (10^{19} cm)	1	1	1	1	1	1	0.01
a_{gr} (μm)	0.2	0.2	0.2	0.2	0.2	0.5	1.
d/g (10^{-14})[a]	1	1	10	100	10	800	10

[a]By number, corresponding to 4 $\times$ 10^{-4} by mass for silicates.

The behaviour at high frequency of the free–free emission is largely dependent on the gas velocities. In Fig. 1, it shows a linear behaviour at low frequencies, then a local maximum, then a maximum at a higher frequency. However, for shock-dominated clouds, the bremsstrahlung shows only a maximum at higher frequencies.

These are the most common types of continuum obtained from a single-cloud model. Very seldom, the line and continuum spectra of the galaxies can be reproduced by single-cloud models; on the other hand, multicloud models are generally required to explain the multiwavelength spectrum and are obtained as a weighted average of the single-cloud models. The characteristics of some of the most common single clouds found in our previous analysis are listed in Table 1. Multicloud models lead to IR bumps wider than blackbody curves. Actually, in some compact objects, e.g. Mrk 3, Mrk 34 and Mrk 78 (Contini & Viegas 2000), dust emission is associated with a single velocity model. This is in contrast with the modelling of the Circinus SED (Contini et al. 1998b), which requires clouds with different velocities contributing at different frequencies in the IR range. This suggests that images of Circinus in the different IR wavelengths may be morphologically very different.

Previous modelling of the representative galaxies with SUMA (e.g. NGC 5252, Circinus, NGC 4151) provided us with hints on which types of clouds are predominant in the NLR (Contini et al. 1998a,b; Contini & Viegas 2000). Adopting an initial grain size of 0.20 μm, it was found that V_s ranges between 100 and 1000 km s^{-1}, n_0 between 100 and 1000 cm^{-3}, log(F_h) between 8 and 13, and D between 0.01 and 10 pc.

The IR bump results from summing up the SED contribution of dusty clouds with different velocities within the NLR, each of them peaking at the corresponding frequency. The maximum of dust emission occurs in the mid-IR for relatively high-velocity clouds. The dust-to-gas ratio may vary from cloud to cloud. From the results obtained for Seyfert galaxies previously modelled by SUMA, we show in Fig. 2, the frequency range corresponding to dust emission associated with a given shock velocity. A similar plot is shown in Fig. 3

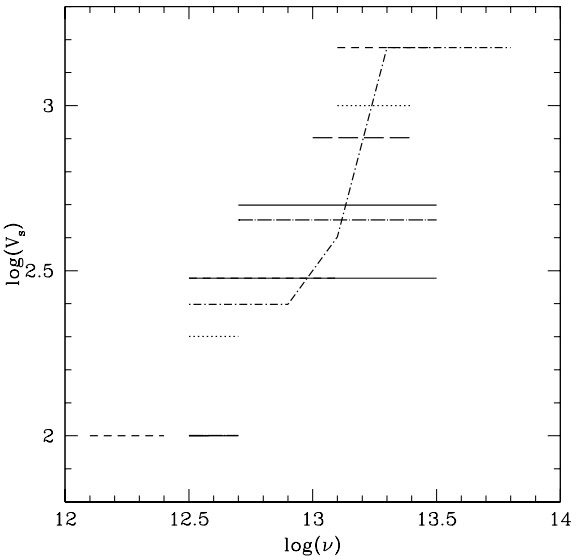

Figure 2. V_s adopted to model the IR data: NGC 7130 (dotted line), NGC 4151 (short-dashed line), NGC 4051 (long-dashed line), Circinus (short-dash–dotted line), NGC 5252 (long-dash–dotted line), NGC 4388 (solid line). Mrk 3, Mrk 34 and Mrk 78 (thin solid line) are selected from Contini & Viegas (2000).

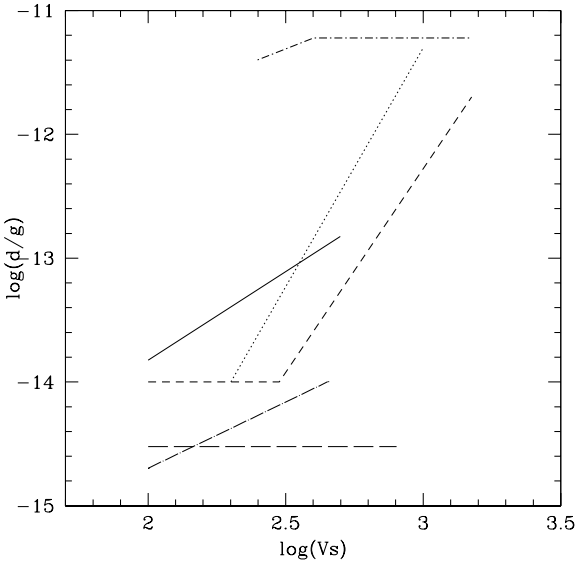

Figure 3. The d/g ratios as a function of V_s adopted to model single galaxies. For description of lines, see Fig. 2.

for d/g. There is a tendency to find higher d/g for higher shock velocities.

2.3 Sputtering of dust grains

In models accounting for the presence of shocks, sputtering changes the initial grain-size distribution, creating a deficiency of small grains with radius $a_{gr} < 50$ Å compared with their pre-shock abundances (Dwek, Foster & Vankura 1996). The altered grain-size distribution depends on shock velocity and on the density of the medium. The sputtering rate increases when the dust is in motion. At temperatures below 10^5 K, all the sputtering is caused by the relative gas–grain motion.

When sputtering is present, the lifetime of grain survival depends on the distance downstream covered by the grains. In order to calculate the critical distance, we use the formula from Shull (1978) which gives the rate of change of grain velocity behind the shock front:

$$\mathrm{d}v_{gr}/\mathrm{d}t = (v_{gr}/2B)(\mathrm{d}B/\mathrm{d}t) - \left(\pi a_{gr}^2/m_{gr}\right)\left(\rho v_{gr}^2\right) - F_{pl}/m_{gr}.$$

Immediately behind the shock front, the grain's gyrovelocity about the magnetic field B is $v_{gr} \sim 3/4V_s$.

The first term on the right-hand side is the rate of change of the grain's gyrovelocity calculated from the conservation of the adiabatic invariant v_{gr}^2/B (Dwek 1981). For a 'frozen in' magnetic field (see Contini & Shaviv 1982):

$$(v_{gr}/2B)(\mathrm{d}B/\mathrm{d}t) = (v_{gr}/2n)(\mathrm{d}n/\mathrm{d}t), \qquad (B = B_0 n/n_0).$$

The second term contains the collisional drag force resisting the grain motion (Dwek 1981) and the third term shows the plasma drag F_{pl} (Shull 1978). Neglecting the plasma drag, if $(v_{gr}/2B)(\mathrm{d}B/\mathrm{d}t) < (\pi a_{gr}^2/m_{gr})(\rho v_{gr}^2)$ the grains decelerate and sputtering is prevented.

Considering that $\mathrm{d}s = \mathrm{d}t\, v_{gas}$ is the differential distance corresponding to lifetime for evolution of the gas throughout a slab, and adopting a silicate density $\sim$3 gr cm^{-3}, we obtain $8/3\ (\mathrm{d}n/n^2)\ a_{gr}/m_{gas} < \mathrm{d}s$. Integrating, the critical distance is given by

$$s\ (\mathrm{cm}) > 10^{16} a_{gr}\,(\mu\mathrm{m})/n(10^4\ \mathrm{cm}^{-3}).$$

To perform the calculations, a cloud is divided into a number of slabs (up to 300) where the physical conditions are considered homogeneous. The geometrical thickness of the slabs is automatically calculated by SUMA according to the gradient of the temperature downstream, in order to calculate as smoothly as possible the distribution of the physical conditions throughout the cloud. The first slabs in the immediate post-shock region show the maximum temperature which depends on V_s. These slabs can be relatively large because recombination coefficients are lower the higher the temperature. The geometrical thickness of the slab closest to the shock front, δ, is therefore determined by the model.

Comparing δ with the critical distance for models with low V_s ($\sim$100 km s^{-1}), a pre-shock density $n_0 = 100$–300 cm^{-3} (corresponding to a density $n \simeq 1000$ cm^{-3} downstream), grains with $a_{gr} = 10^{-5}$ cm are decelerated and hardly sputtered if $\delta > 10^{16}$ cm. For higher n ($>10^4$ cm^{-3}) and a stronger shock ($V_s > 300$ km s^{-1}),

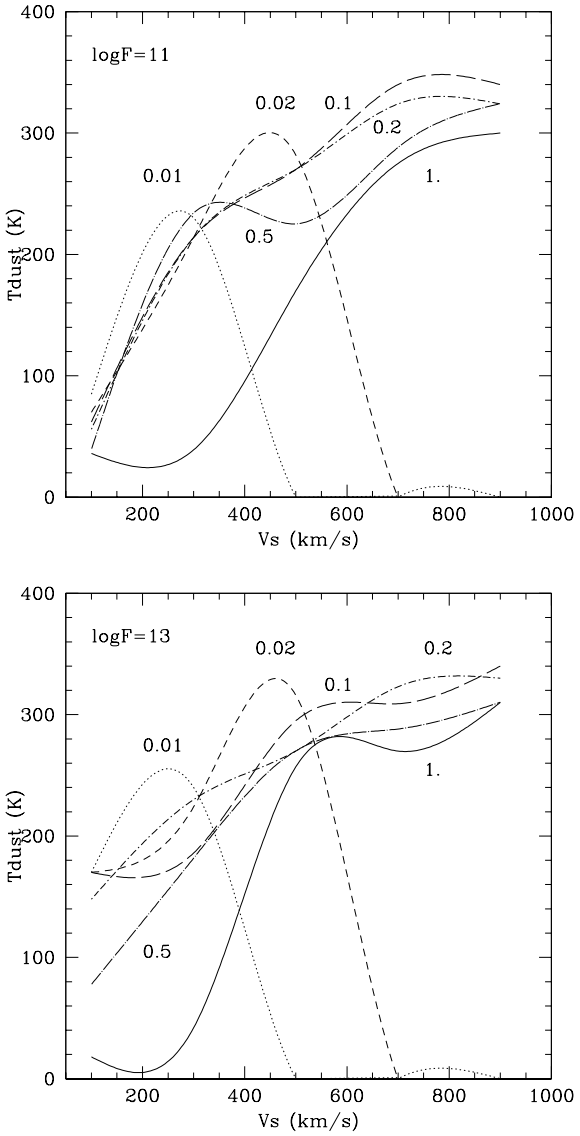

Figure 4. Effective temperature of dust as a function of the shock velocity for different a_{gr} (in μm): dotted lines, $a_{gr} = 0.01$ μm; short-dashed line, 0.02 μm; long-dashed line, 0.1 μm; short-dash–dotted line, 0.2 μm; long-dash–dotted line, 0.5 μm; solid line, 1 μm. The top panel shows log $F_h = 11$ and the bottom panel shows log $F_h = 13$.

the critical distance is $s \simeq 10^{15}$ cm. Actually, the models show slab widths $<10^{15}$ cm for $V_s \leqslant 700$ km s^{-1}. Because the physical conditions in the slab are assumed to be constant, sputtering may be efficient.

For high velocities ($V_s \sim 1000$ km s^{-1}) temperatures are high. Recall that $da_{gr}/dt \propto (T/10^6)^{2.8}$ (Draine & Salpeter 1979), so small grains can be easily destroyed. Therefore, we adopt large grains and very small slabs ($\delta < 10^{13}$ cm) for grain survival. Narrow slabs improve the precision of the calculations. Such slab widths are also much smaller than the critical distances s which are $\sim 10^{16}$ and $\sim 10^{14}$ cm for $n_0 = 300$ and 1000 cm^{-3}, respectively.

Fig. 4 presents the effective temperature of dust calculated for different shock velocities and different grain sizes. Notice that for $V_s \geqslant 700$ km s^{-1} only grains with $a_{gr} > 0.1$ μm survive sputtering and contribute to heating the grains to relatively high temperatures.

3 THE NEAR- AND MID-INFRARED CONTINUUM OF A SAMPLE OF GALAXIES

In this section, we present the modelling of the near-IR and mid-IR continuum of a selected sample of Seyfert galaxies presented by Alonso-Herrero et al. (2003). The continuum data provided by these authors have been subtracted from the light contribution of the background galaxy and are thus the best available data for analysis of the most central AGN emission. For modelling purposes, those objects presenting the widest wavelength coverage and minimum

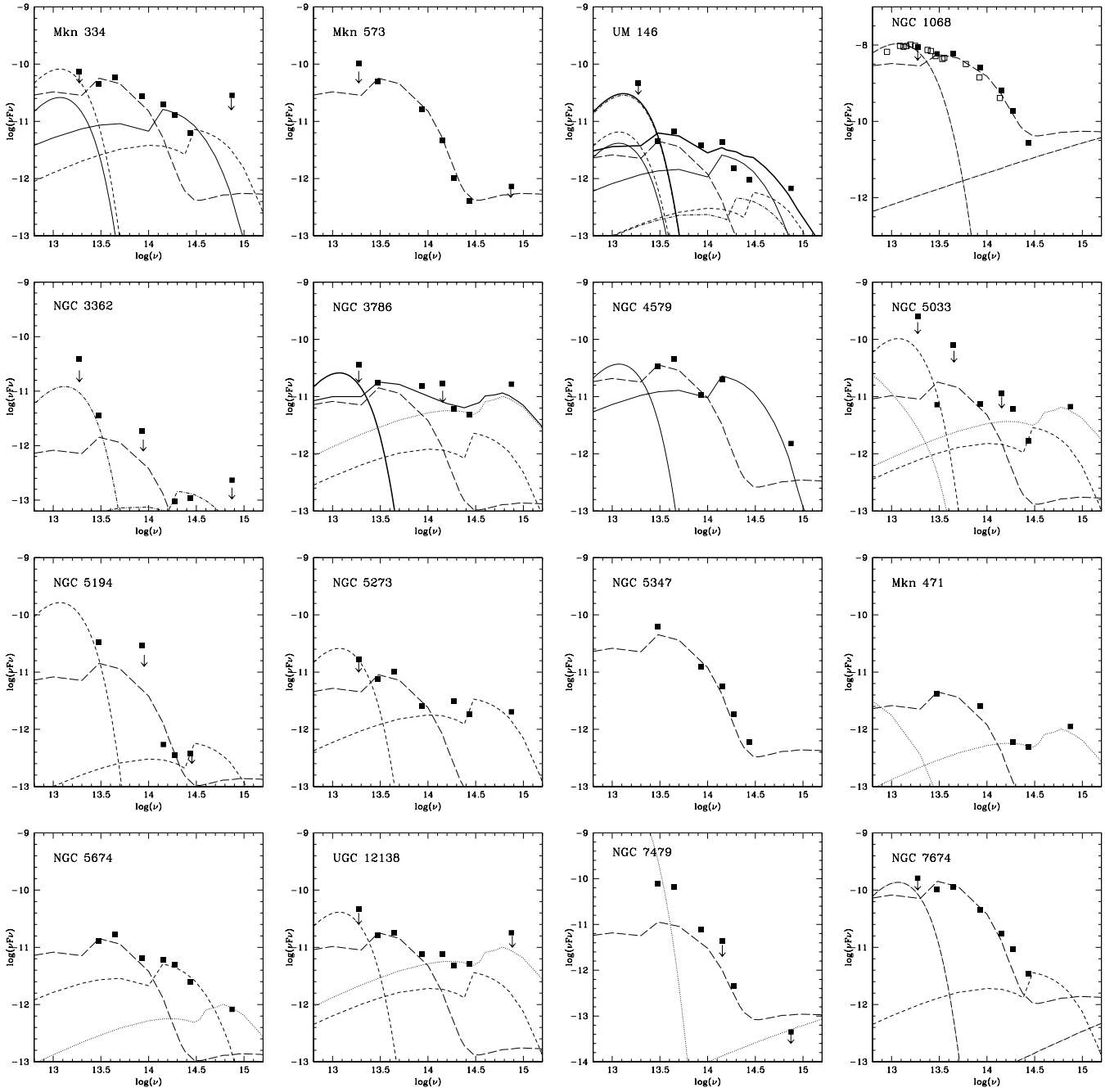

Figure 5. The modelling of selected galaxies from the sample of Alonso-Herrero et al. (2003): Seyfert 1.8–2.

number of upper limits were selected. For NGC 1068, the data set from Rieke & Low (1975) is also included (open symbols). Objects which have previously been modelled in detail are omitted: NGC 4151 (Contini et al. 2002), NGC 4388 (Ciroi et al. 2003), NGC 5252 (Contini et al. 1998a) and NGC 4051 (Contini & Viegas 1999).

In this paper, we try to explain all the galaxies with prototype models. In all cases, clouds with $V_s = 100$ km s^{-1} are present and in most of them $V_s = 500$ km s^{-1} clouds with different d/g also contribute to the fit. In a few cases, higher velocity clouds are also required.

The results produced by multicloud models are shown in Figs 5 and 6 for Seyfert 1.8–2 and Seyfert 1.5–1, respectively. The input parameters of the single-cloud models are listed in Table 1. For each galaxy, the single-cloud models used to fit the continuum are given in Table 2. The covering factors of the clouds are related to the relative weights (see Table 2) which are used to obtain the best-fitting multicloud model. Models M1 and M7 (Table 1) contribute significantly to the fitting of the SED in the near-IR and soft X-ray ranges, respectively. Their continua are shown in Fig. 7. Model M3 is already presented in Fig. 1.

To illustrate the results of multicloud models, in the panels corresponding to UM 148, NGC 3786, Mkn 335 and Mkn 530, the single-model contributions are summed up for the dust emission and for the free–free emission separately, and the best-fitting SED is shown as a thick solid line in Figs 5 and 6. For the other galaxies the domains of the different models are well separated, so only single-cloud models appear in the figure. The summed SED would not change the picture.

We note that, in most cases, the data at the lowest frequency, 16 μm, should be taken as an upper limit, as these are largely contaminated by the host galaxy contribution due to the large ISO aperture. Therefore, the d/g for these clouds, which usually are associated with velocities of about 500 km s^{-1}, is poorly constrained. In two galaxies, Mkn 334 and NGC 3362, the flux at optical frequency is also an upper limit. In NGC 7479, large d/g values ($>8 \times 10^{-12}$) are indicated by the data, in agreement with the upper limit in the optical domain. Data at higher IR frequencies are needed to confirm this d/g value.

In brief, the IR continuum of all the galaxies can be modelled by multicloud models obtained by the weighted sum of different single-cloud models. A fine tune of these results can be obtained by further modelling the emission-line spectra and the overall SED. Nevertheless, from the detailed analysis of a representative number of Seyfert galaxies (Contini et al. 1998a,b, 2002) no dramatic changes for the results of the IR–optical SED are expected.

A comparison between Seyfert 1.8–2 and Seyfert 1.5–1 modelling shows that IR–optical continuum fluxes are generally higher in Seyfert 1.5–1.0; moreover, the flux tends to decrease toward higher frequencies for some Seyfert 2 galaxies. This behaviour is well followed by the models. For all types of galaxies, the continuum between 3 and 10 μm is mainly due to thermal bremsstrahlung by gas with relatively high density and heated by a low-velocity shock (model M1). This indicates that dust emission in this region is relatively low, in contrast with most of the luminous IR galaxies where re-emission by dust dominates at wavelengths even lower than 10 μm (Contini & Contini 2003). Clouds with $V_s \geqslant 500$ km s^{-1} contribute to the SED at higher frequencies. The relative weights of clouds with $V_s \geqslant 500$ km s^{-1} and clouds with $V_s = 100$ km s^{-1} determine the slope of the multicloud continuum SED. On average, the ratios of relative weights for models M1 and M3 (see Table 2), which appear in almost all the galaxies, are higher for Seyfert 1.8–2 (3.7×10^4) than for Seyfert 1.5–1 (1.3×10^4). These models correspond to velocities of 100 and 500 km s^{-1}, respectively. M1 is shock-dominated while M3 is radiation-dominated. From the point of view of the unified model for the AGN, it is expected that high-velocity clouds, reached by a more intense radiation, should play a more significant role in the spectra of broad-line objects, e.g. the NLS1 galaxy Ark 564 (Contini, Rodriguez-Ardila & Viegas 2003a), because the line of sight reaches deeper into the central region, where the high-velocity clouds are. Accordingly, M3 appears in nine out of 16 narrow-line Seyfert but in seven out of eight broad-line objects.

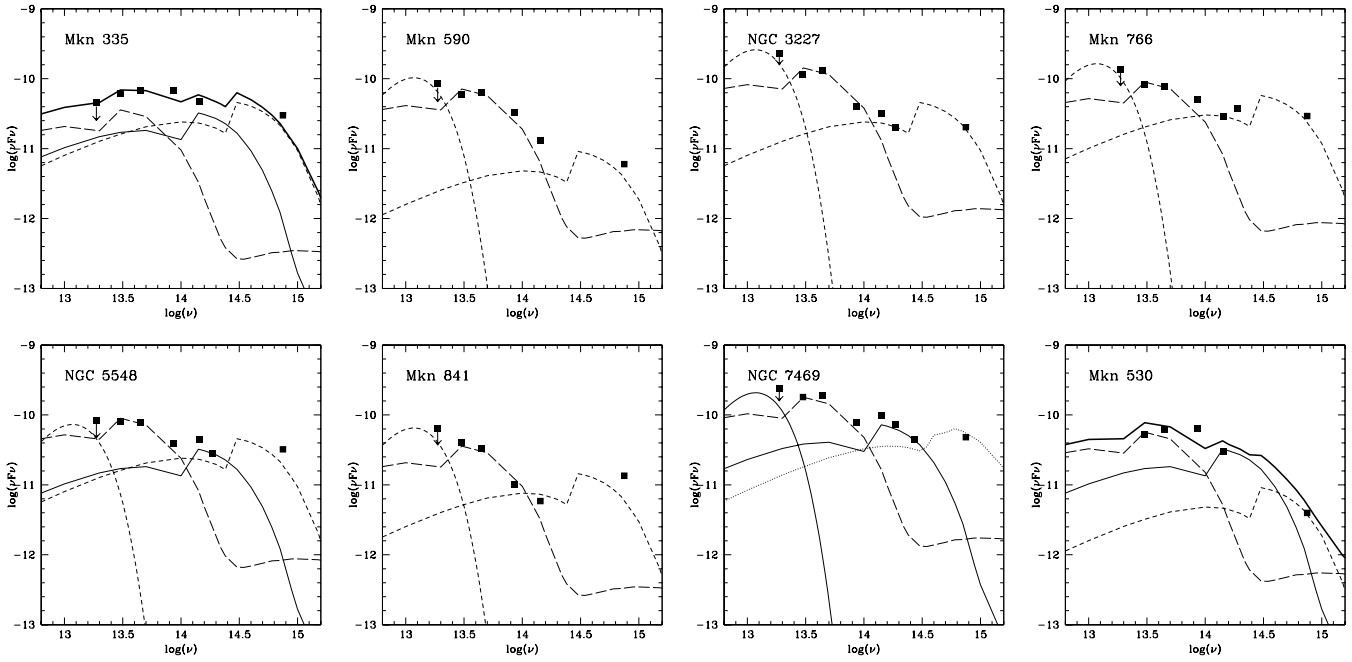

Figure 6. The modelling of selected galaxies from the sample of Alonso-Herrero et al. (2003): Seyfert 1–1.5.

Table 2. The models in Figs 5 and 6.

Galaxy	Seyfert type	Models[a]	Relative weights[b]	CF[c]
Mkn 334	1.8	M1, M2, M3	0, −4.1, −4.6	−8.9
Mkn 573	2.	M1	0	−8.9
UM 146	1.9	M1, M2, M3, M4	0, −3.8, −4.6, −4.1	−10.0
NGC 1068	2.−1.8	M1, M5	0, −2.7	−6.9
NGC 3362	2.	M1, M4	0, −4.	−10.5
NGC 3786	1.8	M1, M3, M7	0, −4.5, −4.3	−9.5
NGC 4579	1.9	M1, M2	0, −3.75	−9.1
NGC 5033	1.9–1.5	M1, M3, M7	0, −4.5, −4.6	−9.4
NGC 5194	2.	M1, M3	0, −5.1	−9.5
NGC 5273	1.9–1.5	M1, M3	0, −4.13	−9.7
NGC 5347	2.	M1	0	−9.0
Mkn 471	1.8	M1, M7	0, −4.8	−10.0
NGC 5674	1.9	M1, M3, M7	0, −4., −5.3	−9.5
UGC 12138	1.8	M1, M3, M7	0, −4.4, −2.1	−9.4
NGC 7479	1.9	M1, M6	0, −3.3	−9.6
NGC 7674	2.	M1, M3, M5	0, −5.3, −3.	−8.5
Mkn 335	1.0	M1, M2, M3	0, −3.6, −3.6	−9.1
Mkn 590	1.0	M1, M3	0, −4.6	−8.8
NGC 3227	1.5	M1, M3	0, −4.2	−8.5
Mkn 766	1.5	M1, M3	0, −3.9	−8.7
NGC 5548	1.5	M1, M2, M3	0, −4., −4.	−8.7
Mkn 841	1.5	M1, M3	0, −4.1	−9.1
NGC 7469	1.0	M1, M2, M7	0, −3.95, −4.6	−8.4
NGC 7603/Mkn 530	1.5/1.8	M1, M2, M3	0, −3.8, −4.5	−8.9

[a]The models are represented in Fig. 5 by the following symbols: M1, long-dashed line; M2, solid line; M3, short-dashed line; M4, short-dash-dotted line; M5, long-dash-dotted line; M6 and M7, dotted line.
[b]In logarithm.
[c]The conversion factor (in logarithm) for each galaxy which accounts for the distance of the emitting clouds to the active centre and for the distance of the galaxy to the Earth. To compare the multicloud models with the data, the weights must be multiplied by the conversion factors (see Contini, Viegas & Campos 2003b).

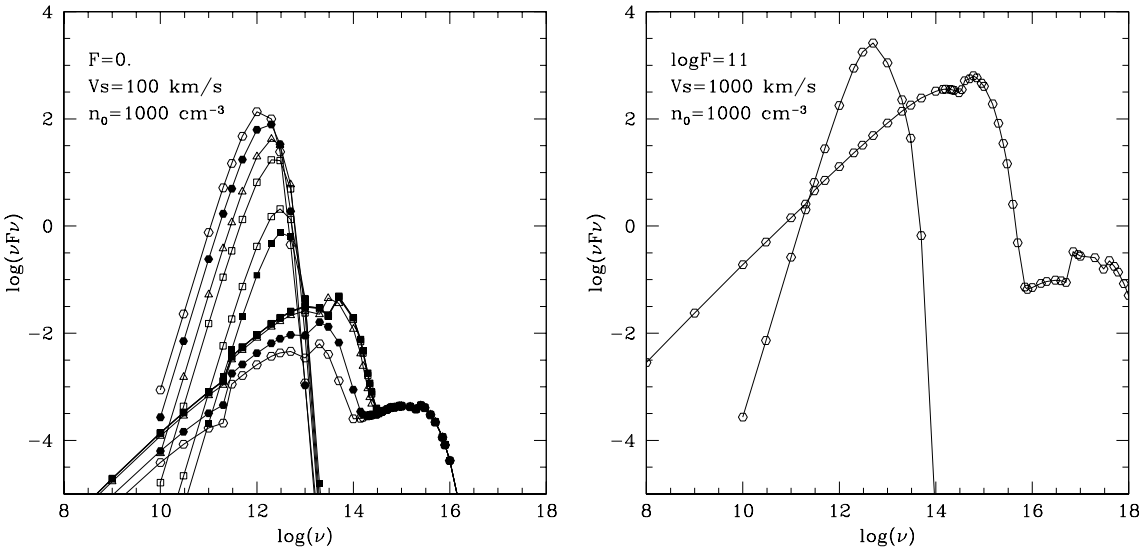

Figure 7. The continua obtained from models M1 (left-hand panel) and M7 (right-hand panel): filled squares, $a_{gr} = 0.01$ μm; open square, $a_{gr} = 0.02$ μm; filled triangles, $a_{gr} = 0.1$ μm; open triangles, $a_{gr} = 0.2$ μm; filled circles, $a_{gr} = 0.5$ μm; open circles, $a_{gr} = 1.0$ μm.

Interestingly, clouds having low V_s and high n_0, basically model M1, are present in all the galaxies. Whether these low-velocity clouds are dusty or not, could only be found out by modelling their FIR nuclear emission, which corresponds to radiation by grains at rather low temperatures. We notice that these types of clouds are difficult to trace in the nebular spectrum because they produce weak lines. Moreover, they were not revealed by previous investigations of AGN spectra because complete data sets between 1.1 and 10 μm were not available yet.

The nature of these clouds is being discussed in detail in the case of the NLS1 galaxy Mrk 766, included in the Alonso-Herrero et al. sample (Contini, Rodriguez-Ardila & Viegas, in preparation). An analysis of the FIR SED is therefore needed to determine the d/g and thus better constrain the modelling. An example of modelling

the complete SED is given in the Appendix, where we present an analytical method to obtain a first representation of the FIR to UV SED of Seyfert galaxies based on our model approach. For this, a more complete grid of models is given.

4 CONCLUDING REMARKS

In the last few years we have shown that composite models which account for the simultaneous effect of photoionization by a central source and by shocks produce a fair representation of the SED of quite a large number of different AGN types, including Seyfert 1.5–2 galaxies, NLS1 galaxies, galaxies where the AGN coexists with starbursts, active galaxies with very extended regions and luminous IR galaxies.

In comparison with other models in the literature, our approach does not resort to any particular dust/gas geometry but explores the possibilities of two mechanisms expected to be present in any AGN, bremsstrahlung and dust reprocessing, to reproduce the IR–optical SED.

We discuss the different contributions to the IR continuum of AGNs considering that both photoionization from the active centre and shocks ionize and heat gas and dust within the surrounding AGN clouds. Collisional processes start to be important in the presence of shocks with velocities of about 100 km s^{-1}. Therefore, dust grains are heated by collision with gas to relatively high temperatures, depending on V_s. Moreover, the grains are sputtered crossing the shock front to different radius depending on the grain initial radius, the plasma density, and the slab width covered by the grains before being decelerated and stopped by collisional drag. The geometrical thickness of the slabs is determined by the assumption that the physical conditions in the slab are constant, and are constrained by the choice of V_s, n_0 and a_{gr} suitable to the NLR conditions.

Observations indicate that there is a gradient of densities and velocities in the NLR, both increasing towards the active centre. In the internal region of the NLR, the radiation should be more intense. We found, however, that in most Seyfert type 2 objects the high-velocity/density clouds are shock-dominated. If these clouds are closer to the centre, the effect of radiation must have been partly cancelled by the effect of an intervening dusty medium. Such dusty medium could be clouds with a very high d/g, which will emit in the FIR. On the other hand, the clouds contributing to intermediate and type 1 Seyfert galaxies are mainly radiation-dominated. These clouds have a direct view of the central radiation as expected from the unified model.

In this paper, the model approach is applied to a sample of galaxies of different Seyfert types for which the best estimates of the nuclear, stellar subtracted, optical–IR SED are available. With a limited range of parameter values (shock velocity, pre-shock density, ionizing flux, grain size and dust-to-gas ratio, which are dictated from our previous detailed modelling of representative Seyfert galaxies), the model results are encouraging as they produce a fair representation of the SED for all Seyfert types. In particular, they easily produce steep IR SED for broad-line type objects.

Further, a first estimate of the dust-to-gas ratio for some of the clouds is provided. Still, FIR data are needed to constrain better those values. Fine tuning of the modelling can be achieved by cross-checking it with the respective nebular spectrum and the SED at other wavelengths. Nevertheless, the analysis of the optical–IR continuum of a sample of galaxies provides a general view of the mechanisms producing the emission, as well as on how they differ in the two types of Seyfert galaxies.

A comparison of Seyfert 1.8–2 with Seyfert 1.5–1 SED models confirms that continuum fluxes are generally higher for Seyfert 1.5–1 and that the flux decrease at higher frequencies can be reproduced for most Seyfert 1.8–2 galaxies. Recall that in multicloud models the single-cloud models are summed up adopting relative weights. We explain, therefore, the flux decrease at higher frequencies by lower relative weights of clouds with higher velocities and/or reached by a strong flux from the active centre.

For all types of galaxies, the continuum between 1 and 10 μm is found to be produced by thermal bremsstrahlung emitted by gas with relatively high density, n_0 (1000 cm^{-3}), heated by a low-velocity shock, V_s (100 km s^{-1}). These clouds produce weak lines and therefore their presence can mostly be accessed from the SED analysis. Because of their low velocity, we expect that dust re-emits in the FIR.

To provide a first analysis of an AGN SED, an analytical method is presented in the Appendix. In general, galaxy continua are explained by multicloud models, leading to extended IR bumps, which must be decomposed into single components. Indeed, the SED profile in the IR of a galaxy depends on the ratio between the dust reradiation peak and the bremsstrahlung emission in the IR, i.e. the dust-to-gas ratios in the single-cloud models, but depends also on the relative weights adopted to sum up the different contributions, which are constrained by the line spectra.

A linear fit of the bremsstrahlung emission (normalized to the value at 12 μm) is adequate for $\log(\nu) < 13.50$, while the emission by dust can be represented by a blackbody (see the Appendix).

ACKNOWLEDGMENTS

We are grateful to an anonymous referee for the comments which helped to improve this paper. This research has been partly supported by the Brazilian agencies FAPESP (00/06695-0) and CNPq (304077/77-1).

REFERENCES

Allen C. W., 1973, Astrophysical Quantities. Athlone Press, London
Alonso-Herrero A., Quillen A. C., Rieke G. H., Ivanov V. D., Efstathiou A., 2003, AJ, 126, 81
Antonucci R. R. J., Miller J. S., 1985, ApJ, 297, 621
Arp H. C., Burbridge E. M., Chu Y., Zhu X., 2001, ApJ, 553, L11
Barvainis R., 1992, ApJ, 400, 502
Benford D. J., 1999, PhD thesis, California Institute of Technology
Blain A. W., Barnard V. E., Chapman S. C., 2003, MNRAS, 338, 733
Carico D. P., Keene J., Soifer B. T., Neugebauer G., 1992, PASP, 104, 1086
Chini R., Kreysa E., Krugel E., Mezger P. G., 1986, A&A, 166, L8
Ciroi S., Contini M., Rafanelli P., Richter G. M., 2003, A&A, 400, 859
Condon J. J., Condon M. A., Broderick J. J., Davis M. M., 1983, AJ, 88, 20
Contini M., Contini T., 2003, MNRAS, 342, 299
Contini M., Shaviv G., 1982, ApSS, 85, 203
Contini M., Viegas S. M., 1999, ApJ, 523, 114
Contini M., Viegas S. M., 2000, ApJ, 535, 721
Contini M., Viegas-Aldrovandi S. M., 1990, ApJ, 350, 125
Contini M., Prieto M. A., Viegas S. M., 1998a, ApJ, 492, 511
Contini M., Prieto M. A., Viegas S. M., 1998b, ApJ, 505, 621
Contini M., Viegas S. M., Prieto M. A., 2002, A&A, 386, 399
Contini M., Rodriguez-Ardila A., Viegas S. M., 2003a, A&A, 408, 101
Contini M., Viegas S. M., Campos P. E., 2003b, MNRAS, 346, 37
de Vaucouleurs G., de Vaucouleurs A., Corwin H. G. Jr., Buta R. J., Paturel G., Fouque P., 1991, Third Reference Catalogue of Bright Galaxies, Version 3.9. Springer, Berlin
Douglas J. N., Bash F. N., Bozyan F. A., Torrence G. W., Wolfe, C., 1996, AJ, 111, 1945
Draine B. T., 1981, ApJ, 245, 880

Draine B. T., Salpeter E. E., 1979, ApJ, 231, 438
Dressel L. L., Condon J. J., 1978, ApJS, 36, 53
Dunne L., Eales S., Edmunds M., Ivison R. Alexander P., Clements D. L., 2000, MNRAS, 315, 115
Dwek E., 1981, ApJ, 247, 614
Dwek E., Foster S. M., Vankura O., 1996, ApJ, 457, 244
Eales S. A., Wynn-Williams C. G., Duncan W. D., 1989, ApJ, 339, 859
Edelson R. A., Malkan M. A., 1986, ApJ, 308, 59
Granato G. L., Danese L., 1994, MNRAS, 268, 235
Granato G. L., Danese L., Franceschini A., 1997, ApJ, 486, 147
Gregory P. C., Condon J. J., 1991, ApJS, 75, 1011
Jarrett T. H., Chester T., Cutri R., Schneider S. E., Huchra J. P., 2003, AJ, 125, 525
Laor A., Draine B. T., 1993, ApJ, 402, 441
Moshir M. et al., 1990, *IRAS* Faint Source Catalogue, version 2.0
Nenkova M., Ivezić Z., Elitzur M., 2002, ApJ, 570, L9
Pier E. A., Krolik J. H., 1992, ApJ, 401, 99
Pier E. A., Krolik J. H., 1993, ApJ, 418, 673
Rieke G. H., Low F. J., 1975, ApJ, 199, L13
Rigopolous D., Lawrence A., Rowan-Robinson A., 1996, MNRAS, 278, 1049
Rowan-Robinson M., 1992, MNRAS, 258, 787
Shull J. M., 1978, ApJ, 226, 858
Siebenmorgen R., Kruegel E., Spoon H. W. W., 2003, A&A, in press
Soifer B. T., Boehmer L., Neugebauer G., Sanders D. B., 1989, AJ, 98, 766
Spinoglio L., Malkan M. A., Rush B., Carrasco L., Recillas-Cruz E., 1995, ApJ, 453, 616
Spinoglio L., Andreani P., Malkan M. A., 2002, ApJ, 572, 105
Vaceli M. S., Viegas S. M., Gruenwald R., Benevides-Soares P., 1993, PASP, 105, 875
Viegas S. M., Contini M., 1994, ApJ, 428, 113
Viegas S. M., Contini M., 1997, in Peterson B. M., Cheng F.-Z., Wilson A. S., eds, IAU Colloquium 159 on Emission Lines in Active Galaxies: New Methods and Techniques. Astron. Soc. Pac., San Francisco
White R. L., Becker R. H., 1992, ApJS, 79, 331
Waldram E. M., Yates J. A., Riley J. M., Warner P. J., 1996, MNRAS, 282, 779
Zwicky F., Herzog E., 1963, Catalogue of Galaxies and of Clusters of Galaxies, Vol. II. California Institute of Technology, Pasadena

APPENDIX A: ANALYTICAL APPROACH

To illustrate the procedure on how to fit the SED of a given galaxy using the present modelling, an example for the case of the SED of Arp 220 is given below. Arp 220 was chosen for two reasons: a rich data set is available for this galaxy and a single-cloud model is enough to provide a good fit of the observed continuum from radio to UV.

The observational data come from the NASA/IPAC Extragalactic Database (NED; Zwicky & Herzog 1963; Dressel & Condon 1978; Condon et al. 1983; Chini et al. 1986; Eales, Wynn-Williams & Duncan 1989; Soifer et al. 1989; Moshir et al. 1990; de Vaucouleurs et al. 1991; Gregory & Condon 1991; Carico et al. 1992; White & Becker 1992; Spinoglio et al. 1995; Douglas et al. 1996; Rigopolous, Lawrence & Rowan-Robinson 1996; Waldram et al. 1996; Benford 1999; Dunne et al. 2000; Jarrett et al. 2003 and from ISOPHOT (Spinoglio, Andreani & Malkan 2002). The SED of Arp 220 (Fig. A1) shows a shape similar to that of model M7 (Table 1, Fig. 7). Bremsstrahlung explains the data in the radio, optical and soft-X ray after removing the background stellar contribution. In the IR, a single blackbody type bump fits the NED (filled squares) data as well as those from ISOPHOT (open squares). The SED can be accounted for with clouds that have $V_s = 1000$ km s^{-1}, $n_0 = 1000$ cm^{-3} and $a_{gr} = 1$ μm. The d/g is determined by shifting the IR bump along the vertical axis by about one order relative to the original model M7. Note that model M7 is originally calculated for $d/g = 10^{-13}$, leading to a too low IR bump (Fig. A1, thin dotted line). The IR data are explained, therefore, with $d/g \sim 10^{-12}$, which is relatively high, in agreement with the fact that Arp 220 is very dusty (Arp et al. 2001) and is also classified as an ultraluminous infrared galaxy (ULIRG).

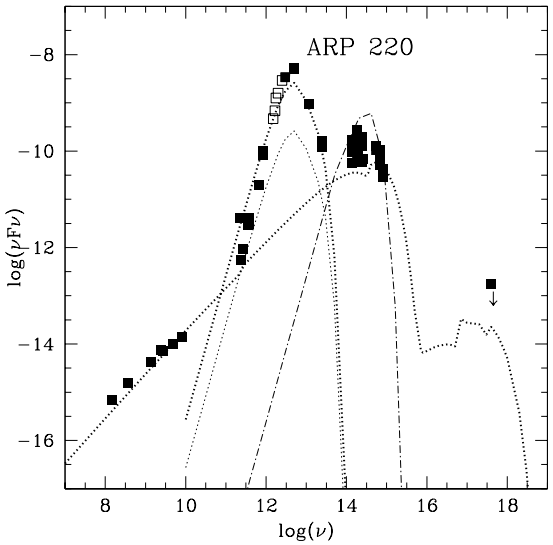

Figure A1. The continuum of ARP 220. Symbols as in Fig. 7.

In order to allow interested readers to use our model approach, a grid of single-cloud models is provided. In all models it is assumed that the shock acts on the edge opposite to that reached by the ionizing photons from the nuclear source, i.e. clouds are moving outwards. The following input parameters are kept constant as follows: the pre-shock density, $n_0 = 300$ cm^{-3}; the geometrical thickness of the cloud, $D = 10^{19}$ cm; the shape of the ionizing radiation; a power law with power index equal to 1.5; the dust-to-gas ratio, $d/g = 10^{-14}$ by number, and the magnetic field, $B_0 = 10^{-4}$ G. The elemental abundances correspond to the cosmic values. On the other hand, the shock velocity varies in the range $100 \leqslant V_s \leqslant 900$ km s^{-1}, the initial radius of the dust grain in the range $0.01 \leqslant a_{gr} \leqslant 1.0$ μm, and the flux at the Lyman limit F_h is 10^{11} and 10^{13} cm^{-2} s^{-1} eV^{-1} (Table A1).

The SEDs of galaxies usually show the old stellar population contribution between about 1×10^{14} and 3×10^{15} Hz. The data are nested between the blackbody curve corresponding to a temperature of $T = 3000$ K (upper limit) and the bremsstrahlung (lower limit). Not always the lower limit is sharply defined. Nevertheless, the lower limit of the data in this range of frequencies roughly constrains the bremsstrahlung. It is, therefore, recommended to use a large range of frequencies, e.g. 10^8–10^{19} Hz to obtain consistent modelling in the different domains (radio, IR, optical, UV and soft X-ray). In Figs A2 and A3 we present the SEDs calculated for models which appear in Table A1. The model SEDs are calculated at the nebula. In order to compare them with the data, the models must be shifted by a factor which depends on the distance of the galaxy, the distance of the cloud from the centre, and the covering factor (see Contini et al. 2003b). Then the bremsstrahlung is adjusted considering the value at the maximum frequency, which depends on V_s and the maximum in the optical range which depends on F_h. The model is constrained by the IR peak frequency, which also depends on V_s.

Notice that the models are calculated with $d/g = 10^{-14}$ by number, so the shift of the IR bump determines the d/g

Table A1. The logarithmic values of νF_ν at 12 μm for the bremsstrahlung and dust emission.

F_h	V_s	a_{gr}	N_{br}	N_{dust}
1e11	100	0.01	−0.1330	5.2637
1e11	100	0.02	−0.1330	−5.4456
1e11	100	0.10	−0.1330	−5.4569
1e11	100	0.20	−0.1330	−5.7847
1e11	100	0.50	−0.1330	−9.6800
1e11	100	1.00	−0.1330	–
1e11	300	0.01	−0.8259	−0.2872
1e11	300	0.02	−0.8279	−0.2419
1e11	300	0.10	−0.6057	−0.1440
1e11	300	0.20	−0.0191	−0.2200
1e11	300	0.50	+1.2140	+0.6850
1e11	300	1.00	−0.9478	−2.5944
1e11	500	0.01	+1.3327	–
1e11	500	0.02	−0.3725	+0.5220
1e11	500	0.10	+1.3327	+0.8780
1e11	500	0.20	+0.7107	+0.7430
1e11	500	0.50	+1.2140	+0.6960
1e11	500	1.00	+1.2978	+0.9700
1e11	700	0.01	+2.2402	–
1e11	700	0.02	+2.3586	–
1e11	700	0.10	+2.3586	+1.7931
1e11	700	0.20	+1.8468	+1.4480
1e11	700	0.50	+2.2211	+2.0000
1e11	700	1.00	+2.3220	+2.4300
1e11	900	0.01	+2.5811	–
1e11	900	0.02	+2.5811	–
1e11	900	0.10	+2.4221	+2.2097
1e11	900	0.20	+2.5800	+2.1688
1e11	900	0.50	+2.4221	+1.9556
1e11	900	1.00	+2.5927	+2.7200
1e13	100	all	+0.5297	−0.2506
1e13	300	0.01	+1.4734	+0.2985
1e13	300	0.02	+1.4807	+0.3734
1e13	300	0.10	+1.4818	+0.4438
1e13	300	0.20	+1.4818	+0.3969
1e13	300	0.50	+0.9388	+0.1656
1e13	300	1.00	+1.1007	−2.5953
1e13	500	0.01	+1.4732	–
1e13	500	0.02	+1.4708	+0.5727
1e13	500	0.10	+1.6263	+0.6687
1e13	500	0.20	+1.5026	+1.3632
1e13	500	0.50	+1.5062	+1.1831
1e13	500	1.00	+1.8973	+1.5431
1e13	700	0.01	+2.3270	–
1e13	700	0.02	+2.3339	–
1e13	700	0.10	+2.3307	+1.7810
1e13	700	0.20	+1.8735	+1.4395
1e13	700	0.50	+2.2000	+1.9817
1e13	700	1.00	+2.2968	+2.4134
1e13	900	0.01	+2.3983	–
1e13	900	0.02	+2.4116	–
1e13	900	0.10	+2.3768	+1.4790
1e13	900	0.20	+2.3977	+1.8422
1e13	900	0.50	+2.5062	+2.3490
1e13	900	1.00	+2.5584	+2.7273

characteristic of the cloud. Complex shapes of the bremsstrahlung maximum and of the IR bump imply a composite model, so the other components must be chosen from Figs A2 and A3 and shifted accordingly.

In the following, based on these models, an analytical method is proposed as an alternative for using the SEDs given above. For each model, the free–free and dust emissions are normalized to their respective values at 12 μm. These values [N_{br} and N_{dust} corresponding to the $\log(\nu F_\nu)$ at 12 μm] are listed in Table A1. Each of the models in Table A1 has characteristics F_h, V_s and a_{gr}, for which the corresponding blackbody effective dust temperature T_{dust} is given in Table A2.

On the other hand, a linear fit of the logarithm of the normalized bremsstrahlung emission is obtained for $11.5 < \log(\nu) < \log(\nu_{lim})$. In Table A3 the coefficients for the linear fit (A and B) and $\log(\nu_{lim})$ are listed for each model. As seen in Fig. 1, for high frequencies, the behaviour of the free–free emission depends on the input parameters of the models and is, in general, characterized by two maxima and a minimum value. In Table A4, for each model the frequency and νF_ν are given for those points identified as $\max_1$, $\min_1$, and $\max_2$ (Fig. 1), as well as the flux at $\log\ \nu = 15.0$.

Using the results listed in Tables A1, A2 and A3, the normalized gas emission can be obtained between $11.5 < \log(\nu) < \log(\nu_{lim})$. The continuum from dust normalized (yd_ν) is a blackbody with $T = T_{dust}$, i.e. $yd_\nu = \log(\nu F_\nu/\nu_{12}\ F_{\nu_{12}})$ with $\log(\nu_{12}) = 13.40$, and Planck function in photons cm^{-2} s^{-1}

$$yd_\nu = 3\log(\nu/\nu_{12}) + \log\frac{\exp[h\nu_{12}/(kT_{dust}) - 1]}{\exp[h\nu/(kT_{dust}) - 1]}, \qquad \text{(A1)}$$

where $h/k = 4.80 \times 10^{-11}$. The thermal bremsstrahlung is obtained from the linear fit.

Notice that for $V_s = 100$ km s^{-1} the bremsstrahlung emission is completely independent of a_{gr}. Nevertheless, the effective dust emission varies with a_{gr} for all the models. The effective dust temperature depends on how efficient the sputtering is. In all models the dust-to-gas ratio is kept constant at $d/g = 10^{-14}$. However, in the fitting procedure of a given galaxy, the d/g will be modified to account for the observed IR peaks in the mid-IR and FIR SED, as described below. Note that the importance of dust relative to free–free emissions depends on the d/g parameter, particularly in the near-IR range.

As shown in the previous sections, the IR–optical SED is usually due to two or more types of clouds, each one corresponding to characteristic velocity and grain size. Here, we give the steps that should be followed to obtain a crude fit of the IR SED, as follows.

(i) The continuum above $\log(\nu) \geqslant 13.50$ is used to find the type of cloud (V_s and a_{gr}) explaining the observed data. The free–free emission dominates the continuum in that frequency range. Using Tables A3 and A4, the best model is chosen.

(ii) Once the cloud characteristics are found, T_{dust}, defining the corresponding blackbody curve, is obtained from Table A2.

(iii) Because the two curves are normalized by the respective values at 12 μm, the non-normalized curves must be used to verify the relative importance of dust and free–free, by shifting vertically the blackbody component, which corresponds to finding the d/g for this particular object. Notice that at this point the scale of the vertical axis is defined by the model, and only the shapes of the curves are used.

(iv) The intermediate and FIR emission are then used to obtain other possible dust components (T_{dust}), which will define the types of cloud (V_s, a_{gr}) as well as their relative importance (d/g) by shifting the non-normalized curves vertically. This will also define the corresponding free–free components.

(v) The final step is to determine the relative weights corresponding to each type of cloud to obtain the best fit to the observed flux values.

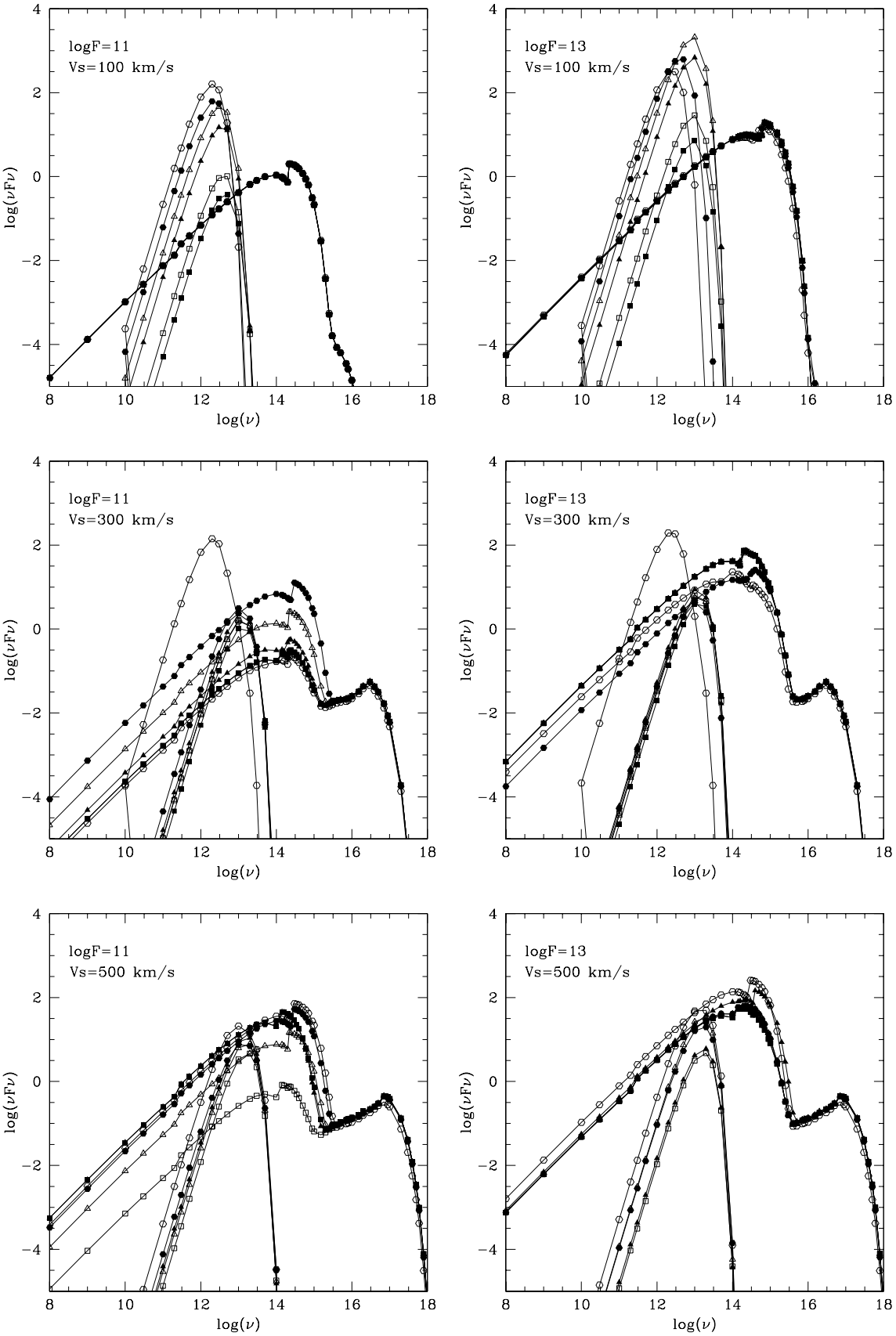

Figure A2. Models. Symbols as in Fig. 7.

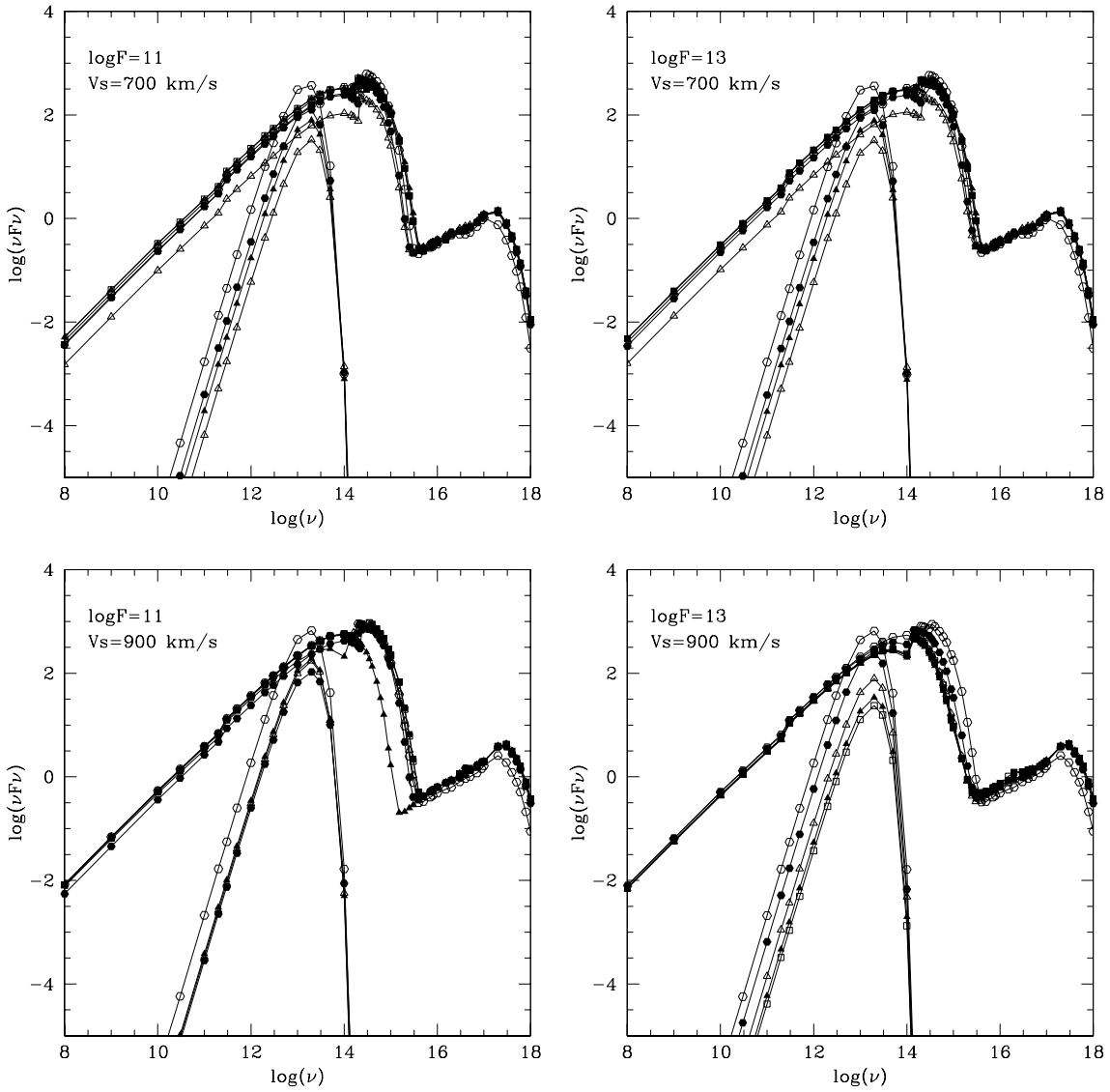

Figure A3. Models. Symbols as in Fig. 7.

Table A2. Effective dust temperature.

$F_h = 1e11$						
V_s/a_{gr}	0.01	0.02	0.10	0.20	0.50	1.00
100	85.	70.	62.	56.	40.	36.
300	230.	214.	214.	214.	234.	39.
500	0.0	282.	270.	270.	225.	170.
700	0.0	0.0	340.	324.	288.	275.
900	0.0	0.0	340.	324.	324	300.
$F_h = 1e13$						
V_s/a_{gr}	0.01	0.02	0.10	0.20	0.50	1.00
100	170.	170.	170.	148.	78.	18.
300	240.	224.	186.	230.	182.	42.
500	0.0	316.	295.	270.	270.	257.
700	0.0	0.0	309.	323.	288.	270.
900	0.0	0.0	340.	330.	310.	310.

Table A3. Linear fit to the logarithm of the normalized bremsstrahlung emission: $y = A \log(\nu) + B$.

F_h	V_s	$\log(\nu_{lim})$	A	B
1e11	100	13.30	0.77	−10.42
1e11	300	13.10	0.80	−10.61
1e11	500	13.10	0.80	−10.60
1e11	700	13.30	0.75	−10.05
1e11	900	13.30	0.76	−10.15
1e13	100	13.40	0.82	−10.98
1e13	300	13.40	0.76	−10.15
1e13	500	13.40	0.76	−10.14
1e13	700	13.30	0.81	−10.76
1e13	900	13.30	0.77	−10.24

Table A4. Characteristics of the bremsstrahlung emission for $\log(\nu) > 13.50$.

F_h	V_s	a_{gr}	max_1	min_1	max_2	Last
1e11	100	all	14.00/+0.033	14.28/−0.142	14.36/+0.344	15.00/−0.654
1e11	300	0.01	13.90/+0.123	14.20/+0.079	14.36/+0.382	15.00/−0.664
1e11	300	0.02	13.90/+0.123	14.20/+0.079	14.36/+0.382	15.00/−0.664
1e11	300	0.10	13.90/+0.123	14.20/+0.079	14.36/+0.382	15.00/−0.664
1e11	300	0.20	14.00/+0.152	14.25/+0.620	14.36/+0.460	15.00/−0.581
1e11	300	0.50	14.00/+0.230	14.37/+0.096	14.48/+0.515	15.00/−0.141
1e11	300	1.00	14.15/+0.230	14.30/+0.118	14.36/+0.475	15.00/−0.568
1e11	500	0.01	13.70/+0.075	14.00/−0.003	14.14/+0.316	15.00/−1.000
1e11	500	0.02	13.70/+0.075	14.00/−0.003	14.14/+0.316	15.00/−1.000
1e11	500	0.10	13.70/+0.075	14.00/−0.003	14.14/+0.316	15.00/−1.000
1e11	500	0.20	14.00/+0.174	14.30/+0.066	14.36/+0.468	15.00/−0.469
1e11	500	0.50	14.00/+0.226	14.38/+0.092	14.48/+0.511	15.00/−0.146
1e11	500	1.00	14.00/+0.256	14.38/+0.170	14.48/+0.558	15.00/+0.044
1e11	700	0.01	14.10/+0.200	14.20/+0.146	14.30/+0.394	15.00/−0.235
1e11	700	0.02	14.10/+0.200	14.20/+0.146	14.30/+0.394	15.00/−0.235
1e11	700	0.10	14.10/+0.200	14.20/+0.146	14.30/+0.394	15.00/−0.235
1e11	700	0.20	14.00/+0.186	14.30/+0.015	14.36/+0.476	15.00/−0.500
1e11	700	0.50	14.00/+0.186	14.30/+0.015	14.36/+0.476	15.00/−0.500
1e11	700	1.00	14.00/+0.217	14.34/+0.062	14.48/+0.472	15.00/−0.270
1e11	900	0.01	14.00/+0.165	14.20/+0.092	14.32/+0.433	15.00/−0.236
1e11	900	0.02	14.00/+0.165	14.20/+0.092	14.32/+0.433	15.00/−0.236
1e11	900	0.10	13.76/+0.058	14.00/−0.098	14.16/+0.295	15.00/−1.800
1e11	900	0.20	14.99/+0.200	14.32/+0.084	14.40/+0.490	15.00/−0.314
1e11	900	0.50	14.99/+0.200	14.32/+0.084	14.40/+0.490	15.00/−0.314
1e11	900	1.00	14.99/+0.200	14.32/+0.084	14.40/+0.490	15.00/−0.314
1e13	100	all	14.36/+0.471	14.70/+0.412	14.85/+0.754	15.00/+0.698
1e13	300	0.01	13.86/+0.128	14.18/+0.058	14.30/+0.400	15.00/−0.504
1e13	300	0.02	13.86/+0.128	14.18/+0.058	14.30/+0.400	15.00/−0.504
1e13	300	0.10	13.86/+0.128	14.18/+0.058	14.30/+0.400	15.00/−0.504
1e13	300	0.20	13.86/+0.128	14.18/+0.058	14.30/+0.400	15.00/−0.504
1e13	300	0.50	14.00/+0.235	14.33/+0.204	14.53/+0.512	15.00/+0.066
1e13	300	1.00	13.70/+0.020	13.85/−0.023	14.06/+0.410	15.00/−0.602
1e13	500	0.01	13.76/+0.117	14.00/+0.075	14.33/+0.269	15.00/−0.560
1e13	500	0.02	13.76/+0.117	14.00/+0.075	14.33/+0.269	15.00/−0.560
1e13	500	0.10	14.36/+0.117	14.54/+0.235	14.60/+0.537	15.00/+0.174
1e13	500	0.20	13.76/+0.117	14.00/+0.075	14.38/+0.320	15.00/−0.469
1e13	500	0.50	13.76/+0.117	14.00/+0.075	14.38/+0.320	15.00/−0.469
1e13	500	1.00	14.00/+0.252	14.38/+0.100	14.48/+0.511	15.00/−0.081
1e13	700	0.01	14.00/+0.174	14.15/+0.135	14.30/+0.412	15.00/−0.310
1e13	700	0.02	14.00/+0.174	14.15/+0.135	14.30/+0.412	15.00/−0.310
1e13	700	0.10	14.00/+0.174	14.15/+0.135	14.30/+0.412	15.00/−0.310
1e13	700	0.20	14.00/+0.191	14.30/+0.040	14.36/+0.459	15.00/−0.409
1e13	700	0.50	14.00/+0.191	14.30/+0.040	14.36/+0.459	15.00/−0.409
1e13	700	1.00	14.00/+0.221	14.34/+0.075	14.48/+0.468	15.00/−0.228
1e13	900	0.01	13.70/+0.056	14.00/−0.508	14.16/+0.282	15.00/−1.400
1e13	900	0.02	13.70/+0.056	14.00/−0.508	14.16/+0.282	15.00/−1.400
1e13	900	0.10	13.70/+0.056	14.00/−0.508	14.16/+0.282	15.00/−1.400
1e13	900	0.20	13.70/+0.056	14.00/−0.508	14.16/+0.282	15.00/−1.400
1e13	900	0.50	13.70/+0.100	14.00/+0.044	14.16/+0.350	15.00/−1.000
1e13	900	1.00	14.00/+0.182	14.20/+0.122	14.30/+0.394	15.00/−0.322

This paper has been typeset from a TEX/LATEX file prepared by the author.